Applied Energy xxx (xxxx) 119839

Contents lists available at ScienceDirect

Applied Energy

journal homepage: www.elsevier.com/locate/apenergy

# Adaptive optimization strategy of air supply for automotive polymer electrolyte membrane fuel cell in life cycle

Zhichao Gong [a], Bowen Wang [a], Yifan Xu [a], Meng Ni [c], Qingchen Gao [a], Zhongjun Hou [d], Jun Cai [d], Xin Gu [d], Xinjie Yuan [d], Kui Jiao [a, b, *]

[a] State Key Laboratory of Engines, Tianjin University, 135 Yaguan Rd, Tianjin 300350, China
[b] National Industry-Education Platform of Energy Storage, Tianjin University, 135 Yaguan Rd, Tianjin, 300350, China
[c] Department of Building and Real Estate, Research Institute for Sustainable Urban Development (RISUD), Research Institute for Smart Energy (RISE), The Hong Kong Polytechnic University, Hung Hom, Kowloon, Hong Kong, China
[d] Shanghai Hydrogen Propulsion Technology Co., Ltd., Unit 10, BLDG 17, Innovation Park, Lane 56, Antuo Rd., Jiading, Shanghai, PR China

ARTICLE INFO

*Keywords:*
Polymer electrolyte membrane fuel cell
Air compressor
Genetic algorithm
Adaptive optimization
Life cycle

ABSTRACT

In this study, an adaptive optimization matching method of the air supply is developed to maintain the high-efficiency operation of the automotive polymer electrolyte membrane fuel cell (PEMFC) system in the life cycle. A 1-D non-isothermal model of the PEMFC stack with 150 kW designed power and a centrifugal air compressor model are developed, considering the fuel cell performance degradation. The genetic algorithm (GA) is used to optimize the overall system efficiency under various output powers to achieve adaptive matching. The 1-D stack model is validated with the experimental test results at two states (before and after 800 h degradation), considering the effect of degradation on the matching strategies. Through the optimization method, the centrifugal air compressor is adaptively matched with the stack of the proposed two states to develop the compressor matching strategies under various stack conditions individually. It is found that the efficiency of the system with this optimized method is 3.8% higher than that of the system without an optimized method under the full system power range. In addition, the new matching strategy between the air compressor and the stack after degradation is exploited by the adaptive optimization method. With the help of this method, the efficiencies of the system and the stack are 5.7% and 2.9% higher than that of the matching strategy without adaptive updating. It is shown that this adaptive optimization method not only improves the output efficiency of the stack but also reduces the additional parasitic power consumed by the compressor.

## 1. Introduction

Polymer electrolyte membrane fuel cells (PEMFCs) utilize the electrochemical reaction of hydrogen and oxygen to produce electricity [1,2]. Because of its advantages of zero-emission, high efficiency, high power density, the PEMFC is regarded as one of the most potential energy conversion devices for automotive applications [3,4]. Extensive efforts are needed to further reduce the cost and improve the durability of PEMFC for large scale commercialization [5,6].

A comprehensive PEMFC system includes the air supply subsystem, hydrogen supply subsystem, temperature control and humidifier subsystem, and fuel cell stack [7,8]. The system performance is determined not only by the stack but also by various auxiliary subsystems, making system optimization much more sophisticated [9,10]. As the most important component in the air supply subsystem, the air compressor affects the performance of the PEMFC system materially [11]. The air compressor is a mechanical device with a relatively slow response, which could cause a significant time delay during the air supply process [12,13]. When the load current density changes suddenly, it may cause cathode oxygen starvation, reducing the cells' output voltage further and even accelerating the decay of fuel cell life [14]. During the operation of the fuel cell system, reasonable pressure and flow rate of the air compressor are required to maintain the high efficiency of the fuel cell system [15]. In general, when an automotive stack is in road use, the fuel cell vehicle unavoidably requires frequent acceleration and deceleration, causing the stack to be subjected to variable load conditions for extended periods, resulting in the stack's degradation [16]. As the fuel cell performance degrades, the exact matching strategy for the air compressor as before will increase the additional power consumption of the system, leading to the reduction of the fuel cell system performance and

* Corresponding author at: State Key Laboratory of Engines, Tianjin University, 135 Yaguan Rd, Tianjin 300350, China.
*E-mail address:* kjiao@tju.edu.cn (K. Jiao).

https://doi.org/10.1016/j.apenergy.2022.119839
Received 14 April 2022; Received in revised form 22 July 2022; Accepted 9 August 2022
0306-2619/© 20XX

accelerating the degradation of the fuel cell life. To address these issues, it is essential to design an adaptive matching method for the PEMFC system that can be used to optimize the air compressor over the entire life cycle of the fuel cell. The matching between the air compressor and the fuel cell is to provide the appropriate amount of compressed air to the fuel cell at a particular speed according to the different output power requirements of the fuel cell, resulting in a high output efficiency of the fuel cell system.

Excellent fuel cell air supply management is a key factor in achieving ideal fuel cell system operating conditions. The air compressor is the most important component of the air supply subsystem, and the appropriate amount of air supply can significantly improve the efficiency and performance of the system. Recently, the PEMFC and air compressor modeling methods have been widely proposed to investigate the design and control strategy of PEMFC system. Yang et al. [17] developed a comprehensive stack model based on the integration of a multiphase stack model and a flow distribution model. The flow distributions and transport processes are considered. Shamardina et al. [18] expounded the transport phenomena across the membrane and the oxygen depletion along the flow channels in the multiphase PEMFC model. However, the effect of membrane water content on the conductivity was ignored. Deng et al. [19] proposed a nonlinear autoregressive moving average with exogenous inputs (NARMAX) to develop a linear time-varying equivalent model for an air compressor and employed recurrent neural networks to estimate the time-varying parameters of the NARMAX model. Zhang et al. [20] presented a 3-D multi-objective and multi-point aerodynamic optimization and data mining method to create a high-performance centrifugal compressor. The optimization significantly improved the aerodynamic performance of the compressor.

Over the past few years, various control strategies for the air supply subsystem composed of air compressors were proposed to effectively regulate the oxygen excess ratio (OER) of the fuel cell to avoid oxygen starvation and saturation. Zakaria et al. [21] proposed an algebraic-observer-based output-feedback controller for the PEMFC air compressor to estimate and regulate the OER in finite time properly. This controller had finite-time convergence and high computational efficiency. A novel approach to the analysis and controller design of a fuel cell gas supply subsystem was proposed by Liu et al. [22] to control the OER of the air compressor. Based on the model analysis, the similarity of the system to the PEM fuel cell gas supply subsystem was demonstrated. PEMFC air supply subsystem is commonly affected by system uncertainty variables. To maintain optimal net power, Wang et al. [23] developed an observer-based discrete adaptive neural network controller to control the OER of the PEMFC air supply subsystem. Proportional integral derivative (PID) control is extensively employed in the industrial control field because of its excellent robustness and reliability. The performance of PID control can be improved by artificial intelligence methods (e.g., neural networks and fuzzy logic). A fuzzy PID hybrid controller was presented to adjust the oxygen excess rate to prevent oxygen deficiency and the fuel cell stack deterioration [24]. Sun et al. [25] employed active disturbance rejection control, which is able to handle the various difficulties in a data-driven manner. The control performance could be improved under varying operating conditions with less control effort and less wear to the compressor. The above research primarily focuses on the short-term control of the fuel cell, with little research into the design and matching strategies of the air supply system to the PEMFC in the life cycle. However, a suitable matching strategy of the air compressor to fuel cell is the fundamental goal of air compressor design and development.

In the present study, an adaptive optimization method based on a stochastic algorithm for air compressors is developed for the first time. The proposed method couples the GA with the physical model of the PEMFC system to develop the adaptive matching model, which optimizes the efficiency of the fuel cell system under various output powers. The physical model is validated by the experimental data of the Hydrogen Propulsion Technology Company's latest generation M4 stack. The air compressor matching status is adaptively optimized under two states, fresh from the factory and after 800 h degradation, to develop matching strategies of air compressor for automotive PEMFC in the life cycle. As a result, the design objectives are provided to the centrifugal air compressor for design and optimization.

## 2. Methods

### 2.1. PEMFC stack model

The schematics of the comprehensive PEMFC system and the computational domain of the stack model are shown in Fig. 1. The stack properties and operating conditions are given in Table 1. The designed power is around 150 kW. The structure of the fuel cell component includes anode and cathode channels (ACH/CCH), gas diffusion layers (AGDL/CGDL), microporous layers (AMPL/CMPL), catalyst layers (ACL/CCL), and polymer electrolyte membrane (MEM). The governing equations are solved numerically to predict the stack performance rapidly. Electrochemical, fluidic, and thermal physical phenomena are also considered, and the model can accurately describe the multi-

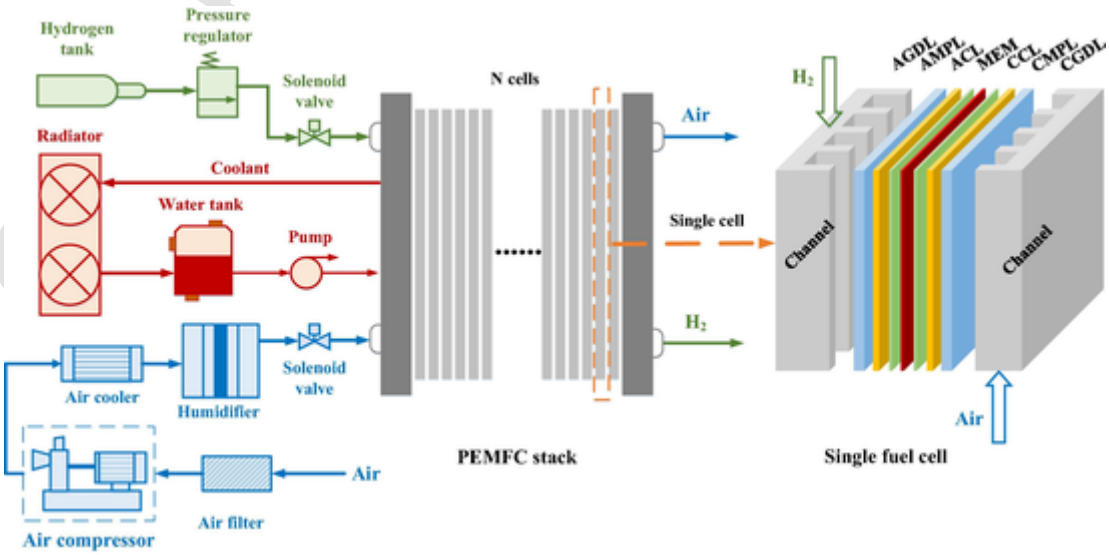


**Fig. 1.** Schematics of the comprehensive PEMFC system and a single PEMFC with the structure of each cell component.

**Table 1**
Physical parameters and operating conditions.

| Parameters | Symbol | Unit | Value |
|---|---|---|---|
| Designed power of stack | $P_{fc}$ | kW | 150 |
| Number of single cells | $N$ | NA | 370 |
| Reaction area | $A_{act}$ | $m^2$ | 0.03 |
| Operating temperature [26] | $T$ | K | 353.15 |
| Height, and width of channel [27] | $W, d$ | mm | 1 |
| Thickness of GDL, MPL, CL, MEM | $\delta_{GDL}, \delta_{MPL}, \delta_{CL}, \delta_{MEM}$ | mm | 0.3, 0.04, 0.01, 0.0508 |
| Porosity of GDL, MPL, CL [26] | $\varepsilon_{GDL}, \varepsilon_{MPL}, \varepsilon_{CL}$ | NA | 0.6, 0.4, 0.3 |
| Contact angle of GDL, MPL, CL [27] | $\theta_{GDL}, \theta_{MPL}, \theta_{CL}$ | ° | 120, 110, 95 |
| Intrinsic permeability of GDL, MPL, CL [27] | $K_{GDL}, K_{MPL}, K_{CL}$ | $m^2$ | $1.0 \times 10^{-11}$, $1.0 \times 10^{-12}$, $1.0 \times 10^{-13}$ |
| Ionomer volume fraction in CL | $\omega$ | S $m^{-1}$ | 0.4,0.4 |
| Sherwood number | $Sh$ | NA | 4.86 |
| Relative humidity of inlet fuel/air | $RH_a, RH_c$ | NA | 1.0,1.0 |
| Dry membrane density | $\rho_m$ | kg $m^{-3}$ | 1980 |
| Equivalent weight of membrane | $EW$ | kg $mol^{-1}$ | 1.1 |
| Anode/cathode reference current density | $j^{ano}_{0,ref}, j^{cat}_{0,ref}$ | A $m^{-2}$ | $3 \times 10^{11}$ ,$1 \times 10^{5}$ |
| $H_2/O_2$ reference concentration | $c_{H_2,ref}, c_{O_2,ref}$ | mol $m^{-3}$ | 100,100 |
| Entropy change [27] | $\Delta S, \Delta S_a, \Delta S_c$ | J $mol^{-1}$ $K^{-1}$ | −163.3, 89.233, −252.463 |
| Thermal conductivity of GDL, MPL, CL, MEM [27] | $k_{GDL}, k_{MPL}, k_{CL}, k_{MEM}$ | W $m^{-1}$ $K^{-1}$ | 1.7, 129, 100, 0.95 |
| Universal gas constant [34] | $R$ | J $mol^{-1}$ $K^{-1}$ | 8.314 |
| Faraday's constant [34] | $F$ | C $mol^{-1}$ | 96,487 |
| Kinetic transfer coefficient | $\alpha$ | NA | 0.4 |
| $H_2$ diffusivity at reference state [28] | $D_{H_2,ref}$ | $m^2$ $s^{-1}$ | $1.055 \times 10^{-4}$ |
| $O_2$ diffusivity at reference state [28] | $D_{O_2,ref}$ | $m^2$ $s^{-1}$ | $2.652 \times 10^{-5}$ |
| Water vapor diffusivity in anode [28] | $D^a_{vap,ref}$ | $m^2$ $s^{-1}$ | $1.055 \times 10^{-4}$ |
| Water vapor diffusivity in cathode [28] | $D^c_{vap,ref}$ | $m^2$ $s^{-1}$ | $2.982 \times 10^{-5}$ |

physical processes inside the PEMFC. The reaction gas flow rate and the pressure ratio parameters at the cathode inlet of the stack model are provided by the air compressor model. Furthermore, the following assumptions are made about the model:

(1) All gases follows the ideal gas law [26].
(2) The internal layers of the fuel cell are assumed to be isotropic [27].
(3) Polymeric electrolyte membrane is assumed to be impermeable to all gases.
(4) The phase change rate between liquid water and vapor is assumed to be gigantic [27].
(5) Convection in the porous layer is not considered in fluid transport calculation [26].

The proposed model operates with constant current condition and the output power of the stack can be calculated as:

$$P_{fc} = \frac{N \times V \times I \times A_{act}}{1000} \tag{1}$$

where $P_{fc}$ (kW) represents the power output of stack, $N$ is the number of single cells, $I$ (A $m^{-2}$) is the current density, $A_{act}$ ($m^2$) is activation area, $V$ (V) is the fuel cell working voltage, which can be determined as:

$$V = E_{rev} - \eta_{ohm} - \eta_{act,a} - \eta_{act,c} \tag{2}$$

where $E_{rev}$ (V) is the reversible voltage, $\eta_{ohm}$ (V) is the ohmic loss of fuel cell, $\eta_{act}$ (V) is the activation loss.

The reversible voltage can be calculated by the Nernst equation:

$$E_{rev} = \frac{\Delta G}{2F} + \frac{\Delta S}{2F}(T - T_{ref}) + \frac{RT}{2F}\left[\ln\left(p_{H_2,a}\right) + \frac{1}{2}\ln\left(p_{O_2,c}\right)\right] \tag{3}$$

where $\Delta G$(J $mol^{-1}$ $K^{-1}$) is the molar Gibbs free energy change, $F$ (96,485 C $mol^{-1}$) is Faraday's constant, $\Delta S$ (J $mol^{-1}$ $K^{-1}$) is the entropy change, $R$ is the gas constant, $T$ (K) is the surrounding temperature, $T_{ref}$ (K) is the reference temperature, $p_{H_2,a}$ and $p_{O_2,c}$ (atm) are the hydrogen pressure in ACL and oxygen pressure in CCL, respectively.

The ohmic loss is caused by ionic and electronic resistances of fuel cell:

$$\eta_{ohm} = \eta_{ohm,P} + \eta_{ohm,por} + \eta_{ohm,m} = (\Omega_{e^{-1},P} + \Omega_{e^{-1},por} + \Omega_{H^{+1},por} + \Omega_{H^{+1},m})I \tag{4}$$

Where $\eta_{ohm,P}$, $\eta_{ohm,por}$ and $\eta_{ohm,m}$ (V) are the ohmic loss of the bipolar plates, porous layers, and polymer electrolyte membrane, respectively, $I$ (A $m^{-2}$) is the current density, $\Omega_{e^{-1},P}$ and $\Omega_{e^{-1},por}$ ($\Omega$ $m^{-2}$) is the surface resistance for electron transport in polar plates and porous layers, respectively, $\Omega_{H^{+1}}$ ($\Omega$ $m^{-2}$) is the surface resistance for proton transport.

The equation of activation loss can be obtained from the derivation of the Butler-Volmer equation [27]:

$$\eta_{act,a} = \frac{RT}{\alpha nF}\cosh^{-1}\left[\frac{I^2}{4\sigma_m^{eff\,2}\left(\frac{\sigma_m^{eff}+\sigma_s^{eff}}{\sigma_m^{eff}\cdot\sigma_s^{eff}}\right)\frac{RT}{\alpha nF}(1-s)\,j^{ano}_{0,ref}\left(\frac{c_{H_2}}{c_{H_2,ref}}\right)^{r_a}} + 1\right]$$

$$\eta_{act,c} = \frac{RT}{\alpha nF}\cosh^{-1}\left[\frac{I^2}{4\sigma_m^{eff\,2}\left(\frac{\sigma_m^{eff}+\sigma_s^{eff}}{\sigma_m^{eff}\cdot\sigma_s^{eff}}\right)\frac{RT}{\alpha nF}(1-s)\,j^{cat}_{0,ref}\left(\frac{c_{O_2}}{c_{O_2,ref}}\right)^{r_c}} + 1\right]$$

where $\eta_{act,a}$ and $\eta_{act,c}$ (V) are the activation overpotential of anode and cathode, $\alpha$ is the charge transfer coefficient, $j_{0,ref}$ (A $m^{-2}$) is the reference current density, $c_{H_2,ref}$ and $c_{O_2,ref}$ (mol $m^{-3}$) are the reference hydrogen concentration and oxygen concentration, respectively.

The diffusion of hydrogen and oxygen in the porous layer follows Fick's law:

$$J_i = -D_i^{eff}\nabla C_i \tag{7}$$

The hydrogen concentration in the anode catalyst layer can be calculated as:

$$\frac{\left(c^{H_2}_{MPL-CL} - c^{H_2}_{CL-PEM}\right)D^{eff}_{H_2,CL}}{\delta_{CL}} = \frac{I}{2F} \tag{8}$$

where $c^{H_2}_{MPL-CL}$ and $c^{H_2}_{CL-PEM}$ (mol $m^{-3}$) are the hydrogen concentration at the interface in the anode, $D^{eff}_{H_2,CL}$ ($m^2$ $s^{-1}$) is the effective diffusivity of hydrogen in the anode catalyst layer, which is corrected by

Bruggeman to $D^{\text{eff}}_{\text{H}_2,\text{CL}} = \left(\varepsilon_{\text{CL}}(1-s)\right)^{1.5} D_{\text{H}_2}$, $\delta_{\text{CL}}$(m) is the thickness of the catalyst layer.

The oxygen concentration in the cathode catalyst layer can be calculated as:

$$c^{\text{O}_2}_{\text{CL}} = \frac{c^{\text{O}_2}_{\text{MPL-CL}} + c^{\text{O}_2}_{\text{CL-PEM}}}{2} \tag{9}$$

where $c^{\text{O}_2}_{\text{MPL-CL}}$ and $c^{\text{O}_2}_{\text{CL-PEM}}$ (mol m$^{-3}$) are the hydrogen concentration in the cathode, $D^{\text{eff}}_{\text{O}_2,\text{CL}}$ (m$^2$ s$^{-1}$) is the effective diffusivity of hydrogen in the anode catalyst layer. The governing equations of reaction gas in the diffusion layer, microporous layer and channel can be solved similarly.

The electro-osmotic drag (EOD) and diffusion of membrane water are considered in the mode of water transport across the membrane. The EOD coefficient $n_d$ represents the number of water molecules that accompany each proton across the membrane from the anode to the cathode:

$$n_d = \frac{2.5\lambda}{22} \tag{10}$$

The diffusivity of membrane water $D_{\text{m}}$ can be calculated as [28,29]:

$$D_{\text{m}} = \begin{cases} 2.69266\times10^{-10} & \lambda \leqslant 2 \\ 10^{-10}\exp\left[2416\left(\frac{1}{303}-\frac{1}{T}\right)\right]\left[0.87(3-\lambda)+2.95(\lambda-2)\right] & 2< \\ 10^{-10}\exp\left[2416\left(\frac{1}{303}-\frac{1}{T}\right)\right]\left[2.95(4-\lambda)+1.642(\lambda-3)\right] & 3< \\ 10^{-10}\exp\left[2416\left(\frac{1}{303}-\frac{1}{T}\right)\right]\left(2.563-0.33\lambda+0.0264\lambda^2-0.00067\right. & \end{cases}$$

where $\lambda$ is the membrane water content in the catalyst layer. The equilibrium water content was measured by Zawodzinski et al. [29] as a function of water activity for the membrane:

$$\lambda = \begin{cases} 0.043+17.81a-39.85a^2+36.0a^3 & 0\leqslant a\leqslant 1 \\ 14.0+1.4(a-1) & 1<a\leqslant 3 \end{cases} \tag{12}$$

$$a = RH + 2s = \frac{P_{\text{H}_2\text{0}}}{P_{\text{sat}}} + 2s \tag{13}$$

where $a$ is water activity, $RH$ is relative humidity, $s$ is local liquid saturation, $P_{\text{sat}}$ (Pa) represents the saturated vapor pressure. The saturated vapor pressure is the critical point between the evaporation and condensation, which can be calculated as follows:

$$\log_{10}\left(\frac{P_{\text{sat}}}{101.325}\right) = -2.1794+0.02953(T-273.15)-9.1837\times10^{-5}(T-2 \\ +1.4454\times10^{-7}(T-273.15)^3$$

The conservation equations for liquid water and membrane water in the anode catalyst layer [30]:

$$\frac{D^{\text{eff}}_{\text{vap,CL}}\left(c_{\text{vap,MPL-CL}}-c_{\text{vap,CL-PEM}}\right)}{\delta_{\text{CL}}} = J_{\text{vap}} \tag{15}$$

$$\frac{\rho_{\text{l}}}{M_{\text{H}_2\text{O}}}\frac{K_{\text{m}}}{\mu_{\text{l}}}\frac{p^{\text{c,l}}_{\text{CL}}-p^{\text{a,l}}_{\text{CL}}}{\delta_{\text{CL}}} + D_m\frac{\rho_{\text{dry}}}{EW}\frac{(\lambda_{\text{ccl}}-\lambda_{\text{acl}})}{\delta_{\text{PEM}}} - \frac{n_d I}{F} = J_{\text{vap}} \tag{16}$$

where $J_{\text{vap}}$ (mol m$^{-2}$ s$^{-1}$) is the flux of vapor, $c_{\text{vap,MPL-CL}}$ and $c_{\text{vap,CL-PEM}}$ (mol m$^{-3}$) are the vapor concentrations at the interface, $D^{\text{eff}}_{\text{vap,CL}}$ (m$^2$ s$^{-1}$) is the effective diffusivity of vapor in the catalyst layer, $\rho_{\text{dry}}$ (kg m$^{-3}$) is the density of membrane, $EW$ (kg mol$^{-1}$) equivalent weight of membrane, $\lambda_{\text{acl}}$ and $\lambda_{\text{ccl}}$ are the membrane water content in the anode and cathode catalyst layer.

The conservation equations for liquid water and membrane water in the cathode catalyst layer:

$$\frac{\rho_{\text{l}}}{M_{\text{H}_2\text{O}}}\frac{K_{\text{l,cl}}}{\mu_{\text{l}}}\frac{p^{\text{l}}_{\text{CL-PEM}}-p^{\text{l}}_{\text{MPL-CL}}}{\delta_{\text{CL}}} = J_{\text{l}} \tag{17}$$

$$\frac{n_d I}{F} + \frac{I}{2F} - \frac{\rho_{\text{l}}}{M_{\text{H}_2\text{O}}}\frac{K_m}{\mu_{\text{l}}}\frac{p^{\text{c,l}}_{\text{CL}}-p^{\text{a,l}}_{\text{CL}}}{\delta_{\text{CL}}} - D_m\frac{\rho_{\text{dry}}}{EW}\frac{(\lambda_{\text{ccl}}-\lambda_{\text{acl}})}{\delta_{\text{PEM}}} = J_{\text{l}} \tag{18}$$

where $\rho_{\text{l}}$ (kg m$^{-3}$) is the density of liquid water, $M_{\text{H}_2\text{O}}$ (kg mol$^{-1}$) is the molar mass of liquid water, $^{s}_{\text{ccl}}$ is the volume fraction in cathode catalyst layer, $^{\epsilon}_{\text{ccl}}$ is the porosity of catalyst layer, $K_{\text{l,cl}}$ (m$^2$) is the permeability of catalyst layer, $\mu_{\text{l}}$ (kg m$^{-1}$ s$^{-1}$) is liquid water viscosity, $J_{\text{l}}$ (mol m$^{-2}$ s$^{-1}$) is the flux of liquid water. The water governing equations in the diffusion layer, microporous layer domain can be solved similarly.

The calculated relationship between the capillary pressure $p_{\text{c}}$ and the volume fraction of liquid water $s$ in the porous layers can be calculated by the Leverett equation:

$$p_{\text{c}} = p_{\text{g}} - p_{\text{l}} \tag{19}$$

$$p_{\text{c}} = \sigma_{\text{lq}}\cos\theta\left(\frac{\varepsilon}{K}\right)^{0.5}J(s) \tag{20}$$

$$J(s) = \begin{cases} 1.42(1-s)-2.12(1-s)^2+1.26(1-s)^3 & \theta<90^\circ \\ 1.42s-2.12s^2+1.26s^3 & \theta>90^\circ \end{cases} \tag{21}$$

where $\sigma_{\text{lq}}$ (N m$^{-1}$) is surface tension coefficient, $\theta$ (°) is contact angle, the volume fraction of liquid water in each component of the fuel cell $s$ is calculated by hydraulic pressure.

Besides the mass transport process, the proposed non-isothermal model also considers thermal phenomena, which can be calculated by the one-dimensional steady-state heat transfer differential equation:

$$\frac{d}{dx}\left(k^{\text{eff}}_{\text{i}}\frac{dT}{dx}\right) = Q_{\text{i}} \tag{22}$$

where $Q_{\text{i}}$ (W m$^{-3}$) is the heat source, which corresponds to the heat production of various fractions of the fuel cell, $k^{\text{eff}}_{\text{i}}$ (W m$^{-1}$ K$^{-1}$) is the effective thermal conductivity. The heat source and the effective thermal conductivity can be calculated as:

$$Q_{\text{i}} = \begin{cases} \frac{I^2}{\sigma_{\text{m}}} \text{ (in MEM)} \\ \frac{I^2}{\sigma_{\text{s,i}}}+\frac{I^2}{\sigma_{\text{m,acl}}}+\frac{I\eta_{\text{act,a}}}{\delta_{\text{acl}}}-\frac{IT\Delta S_{\text{a}}}{2F\delta_{\text{s,acl}}} \text{ (in ACL)} \\ \frac{I^2}{\sigma_{\text{s,i}}}+\frac{I^2}{\sigma_{\text{m,ccl}}}+\frac{I\eta_{\text{act,c}}}{\delta_{\text{ccl}}}-\frac{IT\Delta S_{\text{c}}}{2F\delta_{\text{s,ccl}}} \text{ (in CCL)} \\ \frac{I^2}{\sigma_{\text{s,i}}} \text{ (in GDL, MPL)} \end{cases} \tag{23}$$

$$k^{\text{eff}}_{\text{i}} = k_{\text{i}}(1-\varepsilon)^{1.5} \tag{24}$$

The Dirichlet boundary condition is adopted:

$$T_{\text{ach-gdl}} = T_0 \\ T_{\text{cch-gdl}} = T_0 \tag{25}$$

### 2.2. Air compressor model

Centrifugal air compressor is commonly adopted in PEMFC systems because of its advantages of high specific power and efficiency, and the air compressor model of the system is developed by the modeling method of air compressor mass flow characteristics. This method identifies the mass flow rate of the air compressor from its actual operating parameters by coupling the functional equation between pressure,

speed, and mass flow rate. For the air compressor model and the stack model to be coupled better, the molar flow rate (mol $m^{-2}$ $s^{-1}$) of oxygen at the inlet of the single cell is used to characterize the air mass flow rate (kg $s^{-1}$) of the air compressor. The conversion can be determined as:

$$J_{O_2} = \frac{0.21 \times m_{air}}{M_{air} \times A_{act} \times N} \tag{26}$$

where $J_{O_2}$ (mol $m^{-2}$ $s^{-1}$) is the molar flow rate of oxygen at the inlet of the single cell, $m_{air}$ (kg $s^{-1}$) is the air mass flow rate of the air compressor, $M_{air}$ (kg $mol^{-1}$) is the molar mass of oxygen, N is the number of the cells in the stack.

It is well known that the air mass flow rate is affected by the speed and pressure ratio of the air compressor. The mass flow characteristics of the air compressor are shown in Fig. 2. The function between oxygen flow rate, pressure ratio and speed can be derived using the polynomial fitting method from a large sample of data. To improve the accuracy of the fit, the speed and pressure of the samples are centered, and the multinomial coefficients are given in Table. 2..

$$x = \frac{N_{cp} - 6.625\times10^4}{2.422\times10^4},\ y = \frac{p_{cp} - 2.51}{1.088}$$
$$\begin{aligned} J_{O_2} = {} & p_{00} + p_{10}x + p_{01}y + p_{20}x^2 + p_{11}xy + p_{02}y^2 + p_{30}x^3 + p_{21}x^2y \\ & + p_{12}xy^2 + p_{03}y^3 + p_{40}x^4 + p_{31}x^3y + p_{22}x^2y^2 + p_{13}xy^3 + p_{04}y^4 \\ & + p_{50}x^5 + p_{41}x^4y + p_{32}x^3y^2 + p_{23}x^2y^3 + p_{14}xy^4 + p_{05}y^5 \end{aligned} \tag{27}$$

where $N_{cp}$ (r $min^{-1}$) is the speed of the air compressor, $p_{cp}$ (atm) is the pressure ratio.

It should be noted that the surge operating region and the region exceeding the maximum flow rate are also included. The surge line and the maximum flow rate line are fitted for the air compressor boundary:

$$\begin{cases} p_{sur} = -6.338\times10^4 \times J_{O_2}^4 + 4524 \times J_{O_2}^3 - 106.8 \times J_{O_2}^2 + 57.54 \times J \\ p_{max} = -3.094\times10^4 \times J_{O_2}^4 + 1.133\times10^4 \times J_{O_2}^3 - 1341 \times J_{O_2}^2 + 74.61 \end{cases}$$

The efficiency of centrifugal air compressor corresponding to different pressures, speeds and mass flows varies during the operating process. As the two parameters of the compressor mass flow rate characteristics are identified, the other one is also

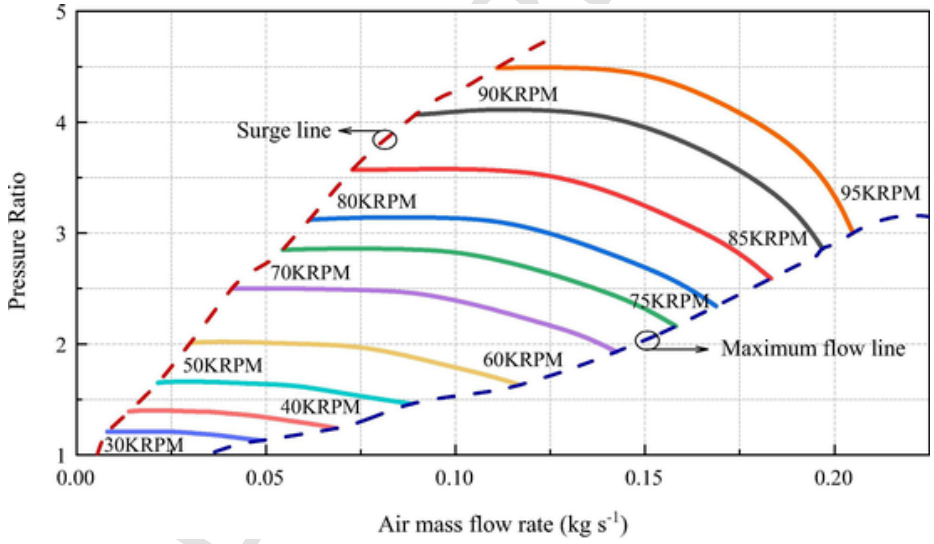


**Fig. 2.** Characteristics of the air compressor.

**Table 2**
Multinomial coefficients of curving fitting results.

| Parameter | Value | Parameter | Value | Parameter | Value | Parameter | Value |
|---|---|---|---|---|---|---|---|
| $p_{00}$ | −0.03913 | $p_{30}$ | 0.9962 | $p_{40}$ | −0.5405 | $p_{50}$ | 0.2404 |
| $p_{10}$ | 0.6498 | $p_{21}$ | −3.255 | $p_{31}$ | 2.633 | $p_{41}$ | −1.372 |
| $p_{01}$ | −0.5311 | $p_{12}$ | 2.832 | $p_{22}$ | −3.886 | $p_{32}$ | 2.874 |
| $p_{20}$ | −1.13 | $p_{03}$ | −0.6863 | $p_{13}$ | 2.116 | $p_{23}$ | −2.604 |
| $p_{11}$ | 2.148 | | | $p_{04}$ | −0.378 | $p_{14}$ | 1.065 |
| $p_{02}$ | −0.8557 | | | | | $p_{05}$ | −0.1649 |

Note: The sum of squares due to error (SSE) is 0.005687, and the coefficient of determination (R-square) is 0.9898.

**Table 3**
Multinomial coefficients of curving fitting results.

| Parameter | Value | Parameter | Value | Parameter | Value | Parameter | Value |
|---|---|---|---|---|---|---|---|
| $q_{00}$ | 0.705 | $q_{30}$ | 0.1554 | $q_{40}$ | −0.1121 | $q_{50}$ | 0.03901 |
| $q_{10}$ | −0.0159 | $q_{21}$ | 0.317 | $q_{31}$ | 0.4251 | $q_{41}$ | −0.2732 |
| $q_{01}$ | 0.02766 | $q_{12}$ | 0.2048 | $q_{22}$ | −0.557 | $q_{32}$ | 0.5521 |
| $q_{20}$ | −0.1549 | $q_{03}$ | 0.00286 | $q_{13}$ | 0.2882 | $q_{23}$ | −0.5373 |
| $q_{11}$ | 0.2493 | | | $q_{04}$ | −0.07993 | $q_{14}$ | 0.292 |
| $q_{02}$ | −0.1342 | | | | | $q_{05}$ | −0.06465 |

Note: The sum of squares due to error (SSE) is 0.005389, and the coefficient of determination (R-square) is 0.9962.

identified. The function between oxygen flow rate, pressure ratio and speed can be derived by using the same method from a large quantity of sample data, and the multinomial coefficients are given in Table 3..

$$x = \frac{N_{cp}-6.625\times10^4}{2.422\times10^4},\ y = \frac{J_{O_2}-0.0606}{0.03776}$$
$$\begin{aligned}\eta_{cp} &= q_{00} + q_{10}x + q_{01}y + q_{20}x^2 + q_{11}xy + q_{02}y^2 + q_{30}x^3 + q_{21}x^2y \\ &+q_{12}xy^2 + q_{03}y^3 + q_{40}x^4 + q_{31}x^3y + q_{22}x^2y^2 + q_{13}xy^3 + q_{04}y^4 \\ &+q_{50}x^5 + q_{41}x^4y + q_{32}x^3y^2 + q_{23}x^2y^3 + q_{14}xy^4 + q_{05}y^5\end{aligned} \quad (29)$$

where $\eta_{cp}$ is the efficiency of the air compressor, the compression of the centrifugal air compressor is regarded as an isentropic process and the power of the air compressor can be calculated as follows:

$$P_{cp} = c_p \frac{T_{cp}}{1000\times\eta_{cp}}\left(p_{cp}^{\frac{\gamma-1}{\gamma}} - 1\right) \quad (30)$$

where $c_p$ (J kg−1 K−1) is the specific heat capacity of air, $\gamma$ is the ratio of specific heat of air.

### 2.3. Power and efficiency of PEMFC system

A comprehensive PEMFC system includes the air supply subsystem, hydrogen supply subsystem, temperature and humidifier subsystem, and fuel cell stack. The air supply subsystem is the largest power-consuming device of the fuel cell system, and the power consumption of the air compressor increases with the power of the stack. The power consumption is also caused by auxiliary components such as the hydrogen circulation pump, water pump and cooling fan, but compared with the power consumption of the air compressor, it is negligible and has little effect on the output power of the fuel cell system. Consequently, in this study, only the coupling between the stack and the air compressor is investigated, while the effects of other auxiliary components are not considered.

The system output power is calculated as the difference between the effective output power of the fuel cell and the parasitic power consumption of the auxiliary components:

$$P = P_{fc} - P_{cp} \quad (31)$$

Efficiency is the most important evaluation indicator of the fuel cell system. The efficiency of the energy conversion process is determined as the ratio of useful energy output to the total energy input. However, the actual fuel cell stack efficiency is much lower than the theoretical efficiency because of the fuel utilization losses and voltage losses due to cell polarization, which can be calculated as:

$$\eta_{fc} = \eta_{fuel}\frac{V}{E_{rev}} \quad (32)$$

where $\eta_{fuel}$ is fuel utilization, which is set as 99% in this study.

The fuel cell system efficiency takes the power consumption caused by the auxiliary components of the fuel cell system into account, and is calculated as follows:

$$\eta = \eta_{fc}\frac{P}{P_{fc}} \quad (33)$$

### 2.4. Stochastic optimization algorithm

A stochastic optimization algorithm, genetic algorithm (GA), is adopted to match the optimal compressor conditions in various power ranges of the fuel cell for improving the system output efficiency in this work. GA is a method to find an approximate optimal solution inspired by a natural evolutionary process [31]. Fig. 3 shows the workflow of the GA, which is generally applied during the optimization process in this work. The initial number of populations generated is set to 1000 and the number of iterations of evolution is set to 100. The current density of the fuel cell stack, the speed, the pressure ratio, and the mass flow rate of the air compressor are the variables to be optimized. The individuals with a higher fitness level in the population are more likely to be selected to reproduce the next generation with optimization, so the best fitness individual is acquired by continuous iteration [32]. The fitness function is used to evaluate the fitness of an individual, and the efficiency of the system predicted by the numerical model is adopted as the fitness function in this paper. In addition, the penalty term is added in the fitness function to increase the elimination possibility of individuals which do not meet the constraints in the selection [33]. To guarantee the prediction accuracy of the numerical model, the output power ranges of the PEMFC system and the cathode stoichiometric ratio for this optimization method should be within the restrictive ranges. The cathode stoichiometry ratio (oxygen excess ratio) range is limited to 1.2–4.0 and the output power of the PEMFC system is divided into a series of ranges in Table. 4. The fitness function can be expressed as:

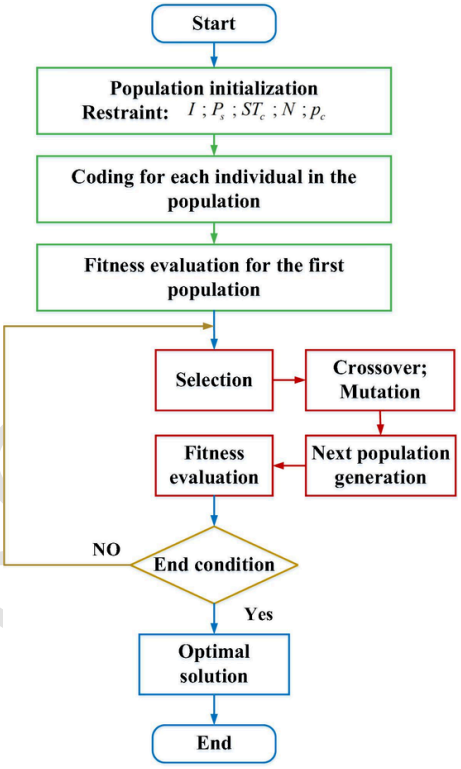


**Fig. 3.** Schematics of the workflow of GA.

**Table 4**
Restrictive ranges of the PEMFC system power in the case generation.

| No. | Lower bound | Upper bound | No. | Lower bound | Upper bound |
|---|---|---|---|---|---|
| 1 | 0 kW | 5 kW | 14 | 65 kW | 70 kW |
| 2 | 5 kW | 10 kW | 15 | 70 kW | 75 kW |
| 3 | 10 kW | 15 kW | 16 | 75 kW | 80 kW |
| 4 | 15 kW | 20 kW | 17 | 80 kW | 85 kW |
| 5 | 20 kW | 25 kW | 18 | 85 kW | 90 kW |
| 6 | 25 kW | 30 kW | 19 | 90 kW | 95 kW |
| 7 | 30 kW | 35 kW | 20 | 95 kW | 100 kW |
| 8 | 35 kW | 40 kW | 21 | 100 kW | 105 kW |
| 9 | 40 kW | 45 kW | 22 | 105 kW | 110 kW |
| 10 | 45 kW | 50 kW | 23 | 110 kW | 115 kW |
| 11 | 50 kW | 55 kW | 24 | 115 kW | 120 kW |
| 12 | 55 kW | 60 kW | 25 | 120 kW | 125 kW |
| 13 | 60 kW | 65 kW | 26 | 125 kW | 130 kW |

$$f = \begin{cases} \eta\left(N, J_{O_2}, p_{\mathrm{cp}}, I\right), & \text{if} \begin{cases} ST_c \in [1.2, 5.0] \\ P \in \left(P_{\text{Lower boundary}}, P_{\text{Upper boundary}}\right] \end{cases} \\ \frac{1}{1000} \times \eta\left(N, J_{O_2}, p_{\mathrm{cp}}, I\right), & \text{else} \end{cases} \quad (34)$$

The GA Optimization Toolbox developed by North Carolina State University is used to conduct the optimization process in the current work. The air compressor parameters and current density are optimized in various intervals of output power to find the best operating conditions for the fuel cell system efficiency, so the matching strategies for the air compressor and fuel cell are developed. As the performance of the stack degrades, the output performance of the degraded system is adaptively updated by the GA. As a result, a new matching strategy between the air compressor and the fuel cell is developed in various output power intervals of the degraded system.

## 3. Results and discussion

### 3.1. Physical model validation

To verify the accuracy of the model, the simulation results of the 1D non-isothermal stack model are compared with the experimental data from the latest generation of M4 stack produced by Shanghai Hydrogen Propulsion Technology Co., Ltd. From these validations, the proposed stack model is confirmed to predict the fuel cell performance with a certain degree of accuracy. As shown in Fig. 4, a comparison of the polarization curve between the experimental data and simulation results is presented in various states (before and after degradation) of the M4 stack. The experimental and simulation data before the degradation of the stack are indicated by red symbols and lines, and the blue symbols and lines are used to characterize the experimental and simulation results after the 800 h degradation test of the stack at variable load conditions. It is obvious that reasonable agreements are achieved with a relative error of less than 2% in the comparison. Meanwhile, compared with the data before and after the 800 h degradation, the output voltage of the stack after the degradation is 7.4% lower than the voltage before the degradation, which is significantly different from the experimental data of the brand-new factory. In this study, the PEMFC model will be calibrated based on the two operating conditions of the stack (before and after the 800 h degradation) and will be adaptively optimized to match the air supply system, respectively. So the air compressor matching strategy for the various states of the stack is developed.

### 3.2. Effect of air compressor parameters on system efficiency

The variation in the characteristics parameters of the compressor significantly affects the PEMFC system efficiency, so the system performance can be greatly improved by a suitable compressor operating condition. The evolution of the system efficiency with current density for various compressor pressure ratios and speeds can be shown in Fig. 5. At the same compressor speed, the stack performance progressively improves with increasing pressure ratio, leading to an improvement in the maximum efficiency of the system. Nevertheless, the increase of pressure ratio reduces the air mass flow with the fixed speed, and the sufficient air flow cannot be provided by the compressor to meet the demands of high current density conditions, resulting in the reduction of limiting current density and the current density corresponding to maximum efficiency. Furthermore, both the pressure ratio and the air mass

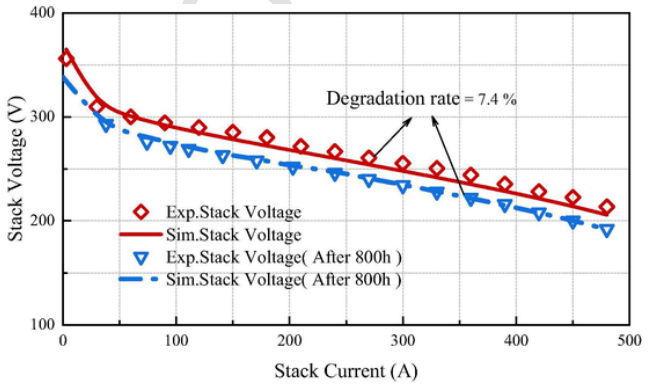


**Fig. 4.** Comparison between simulation results and experimental data of M4 stack.

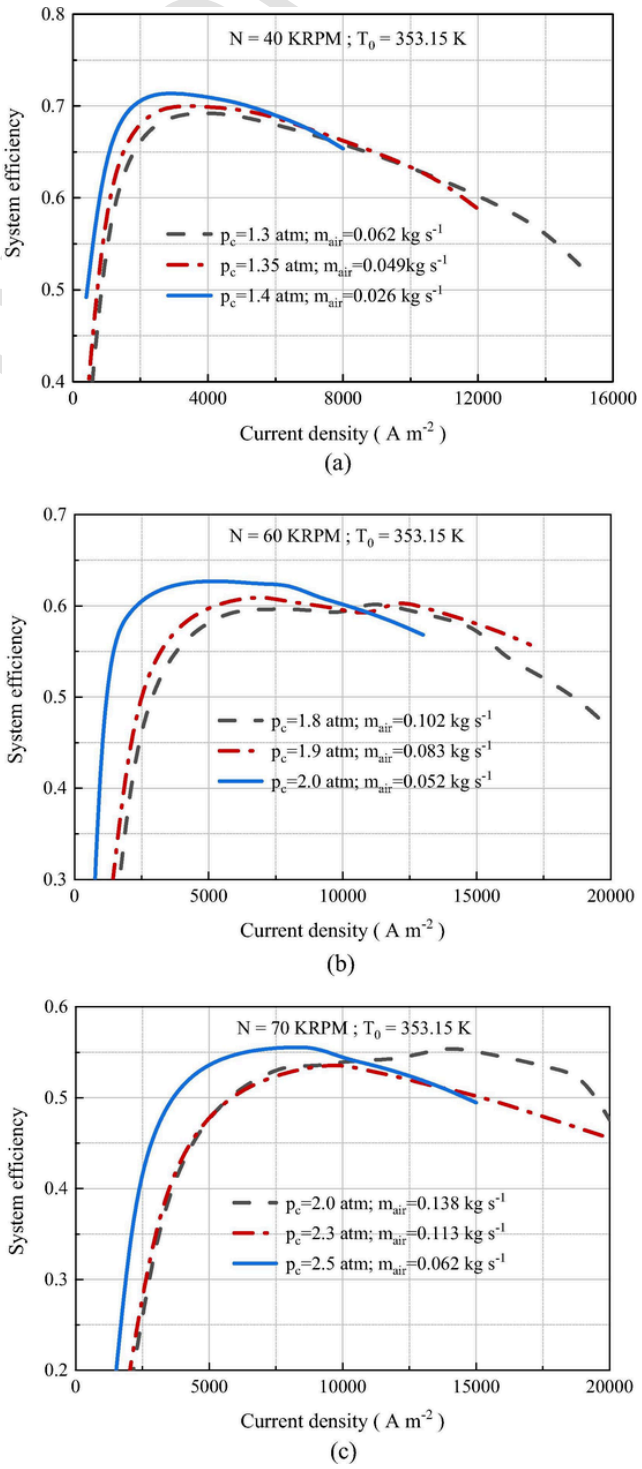


**Fig. 5.** The evolution of the system efficiency with current density for various compressor pressure ratios and speeds.

flow rate are increased with increasing compressor speed, and the performance of the stack is improved because of the high-pressure ratio and the sufficient supply air flow, which is manifested in the increase of the limiting current density. On the contrary, the parasitic power consumption of the air compressor is increased at high speeds, resulting in the reduction of the maximum efficiency of the system.

Fig. 6 shows the evolution of the system efficiency with the speed of the compressor for different cathode stoichiometry ratios and the current density of the stack. The stoichiometric ratio is measured as the relative relationship between the actual gas supply and the reaction rate, the larger the stoichiometric ratio, the more abundant the cell gas. At the same cathode stoichiometry ratio, the air mass flow rate of the air

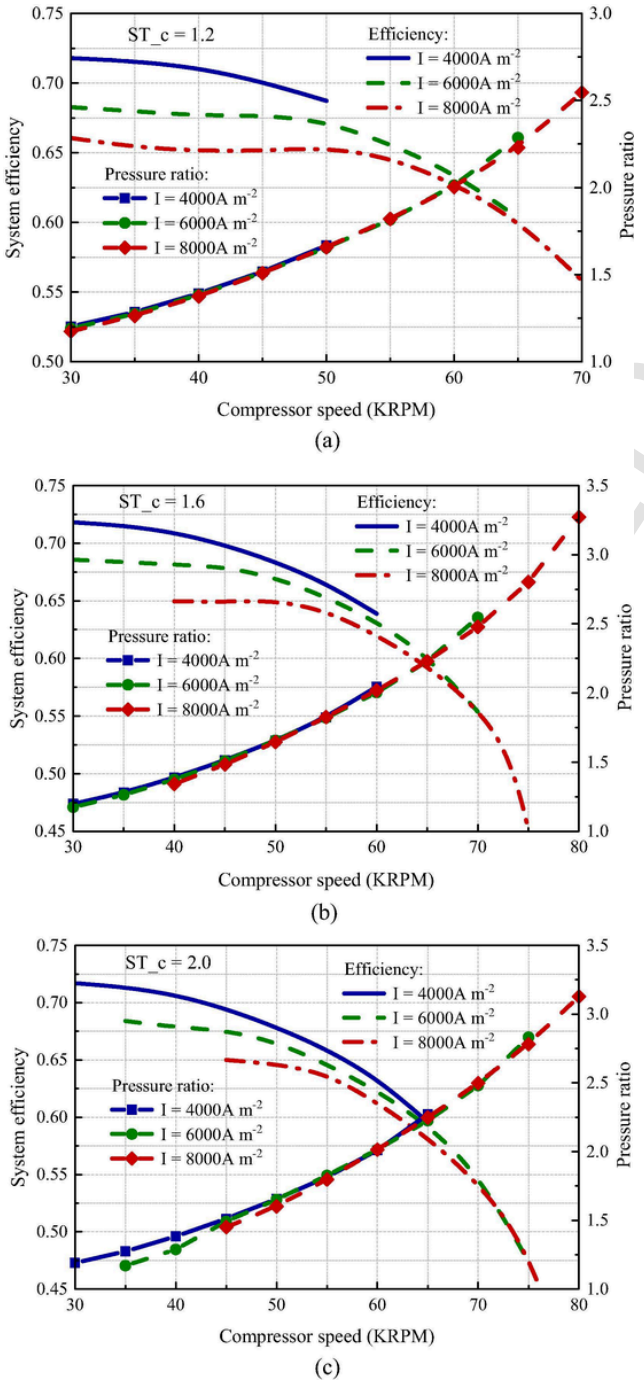


**Fig. 6.** The evolution of the system efficiency and the pressure ratio with the speed of the compressor for different cathode stoichiometry ratios and the current density of the stack.

compressor is increased, and the pressure ratio is reduced with the increasing current density, while the output efficiency of the stack will be lower under the large current density conditions, resulting in the reduction in the maximum efficiency of the system. However, the corresponding pressure ratio is increased as the speed of the compressor rises. Despite of the improvement in the stack performance, the efficiency of the system is reduced due to the power of the compressor. The increase of the cathode stoichiometry ratio means that more air is supplied to the stack by the air compressor, and the speed of the matched compressor is higher under the same current density conditions, but the variation of the optimum system efficiency is not obvious. The effect of compressor characteristics and stack operating parameters on system efficiency is relatively complex and cannot be summarized by a linear relationship. Consequently, it is essential to investigate the matching strategy of the air compressor and the stack to keep the system working in an efficient and orderly operation.

### 3.3. Optimization results

The air compressor is one of the most essential auxiliary components of the PEMFC system. The output power of the stack can be effectively increased by increasing the air inlet pressure and flow rate. Nevertheless, the parasitic power consumption of the air compressor increases with the pressure and flow rate of the air, which decreases the effective output power of the system. In this study, an adaptive optimization method coupling the GA and the system model is employed to find the maximum efficiency of the PEMFC system in different output power ranges by adjusting the inlet flow, pressure ratio and speed of the air compressor as well as the current density of the stack. Furthermore, the adaptive matching strategy between the air compressor and the stack is investigated.

Due to the random generation mechanism of the initial population, the optimal solution by the stochastic optimization algorithm also shows a certain randomness. The number of initial populations is a critical factor that will affect the optimization results. The initial populations and the number of iterations are 1000 and 100, respectively. In this study, the fitness is set as the efficiency of the PEMFC system. The evolution of the best fitness for the system power range of 0–5 kW is shown in Fig. 7(a). The optimization significantly optimizes the best fitness and gradually stabilizes after 30 generations. The system efficiency is improved from 0.7535 to 0.78821 by evolution, an improvement of 4.6% is achieved.

The evolution of the efficiency of the system, stack and air compressor under all system power ranges is shown in Fig. 7(b). The red lines represent the system efficiency before and after optimization. The efficiency of the PEMFC system is significantly raised by GA optimization, with an improvement of 3.8% in overall power ranges. After optimization, the maximum system efficiency can be close to 80% under low current density conditions. In addition, the efficiency of the system and stack will gradually decrease as the output power of the PEMFC system increases. On the contrary, the efficiency of the air compressor is gradually improved as the system power increases. It is well known that the output power of the stack increases with the current density until the maximum output power is achieved, while the output voltage and the efficiency of the stack will decrease with the current density, causing the reduction of the system efficiency.

Fig. 8 shows the most suitable matching of the stack and air compressor operating conditions for various system power output cases. As shown in Fig. 8(a), the power of the stack gradually increases with the requirement of the system output power until the maximum output power of the stack is achieved. Similarly, the current of the stack is positively correlated with the system output power and increases with the requirement of the system power. The optimization results show that the corresponding cathode stoichiometry ratio (oxygen excess ratio) gradually decreases with the growing system power in the low-

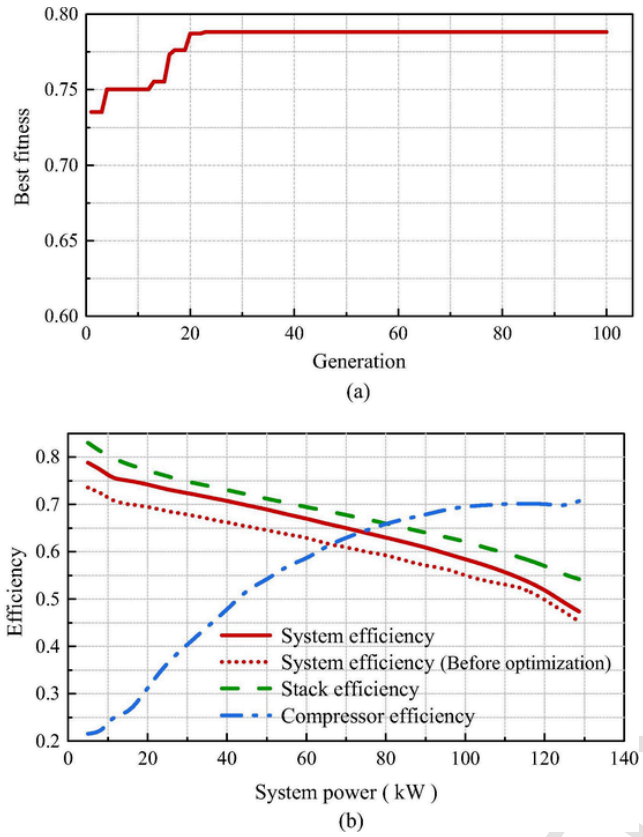


**Fig. 7.** Optimization results by GA, (a) optimization process of best fitness (the maximum system efficiency), (b) evolution of efficiency (system/stack/compressor) under total system power.

power output stage. In contrast, the cathode stoichiometry ratio is stable at around 1.3–1.4 as the required output power is further increased. In this study, the assumption of single cells' consistency is proposed to ensure the efficiency of the model, so the value of the optimization results represents the cathode stoichiometry of the stack. The stoichiometric ratios of the different single cells will vary slightly from each other in actual operating conditions, which is ignored. The optimized air compressor operating conditions are shown in Fig. 8(b), With the increasing system power, the corresponding air compressor speed, pressure ratio, mass flow rate and air compressor parasitic power are rising progressively. Meanwhile, the growth rates of air compressor pressure ratio, mass flow rate and parasitic power are significantly accelerated with the higher demand for system power. Particularly in the condition of system power above 120 kW, more air flow and a higher cathode pressure ratio of the compressor are required, resulting in the acceleration of the corresponding compressor power growth rate.

### *3.4. Adaptive optimization results after degradation*

The performance of the on-board stack is significantly degraded by the long-term varying load conditions during the vehicle driving cycle, so it is not suitable to couple the matching strategy that has not been updated with the stack. In this section, the strategy between the air compressor and stack is adaptively optimized according to the practical degradation state of the stack. And thus, a suitable matching strategy for the air compressor can be developed. The evolution of the air compressor working conditions is further investigated by comparing the strategy before adaptive optimization with the strategy after optimization.

The adaptive optimization results after stack degradation are shown in Fig. 9.Fig. 9(a) shows the evolution of the PEMFC system efficiency between the strategies before and after degradation. Fig. 9(b) shows the evolution of the stack efficiency. Comparing the matching results of the previous matching strategy and the adaptive optimization strategy when the stack is in the 800 h degraded state, it is observed that the system efficiency and the stack efficiency are significantly improved under all-power conditions with the adaptive optimization strategy. Compared with the results of the matching strategy before degradation, the system efficiency is improved by 5.7% and the stack efficiency is improved by 2.9% with the adaptive optimization strategy. The improvement in system efficiency is much more significant than in stack efficiency because the adaptive optimization strategy may improve the output performance of the stack and affect the additional parasitic power consumed by the air compressor.

With the above adaptive optimization method, the evolution of the optimized compressor working conditions is further analyzed. The comparison of the compressor operating conditions with the previous matching strategy and the adaptive optimization strategy is presented in Fig. 10. The matched compressor speed is indicated by the black line and the pressure ratio of the compressor is indicated by the red line. It can be seen that the speed and pressure ratio of the air compressor with the adaptive optimization strategy are much lower at the same output system power compared to the air compressor conditions without the updated strategy, which is particularly obvious when the system power is lower than 100 kW. But as the system output power rises, the air compressor is required to provide higher air inlet pressures and air flow rates to meet the high-power requirements. Consequently, the variation of the mass flow characteristics parameters of the air compressor with the adaptive optimization strategy at high power is not noticeable compared to the previous strategy. Meanwhile, the parasitic power consumption of the air compressor with the adaptive optimization strategy is also lower, which indicates that the matching strategy with adaptive optimization can improve the output efficiency of the stack and reduce the additional parasitic power consumption by the auxiliary components. This method is expected to provide the design reference for the optimization of centrifugal air compressors and system matching.

## 4. Conclusions

In this study, an adaptive optimization matching method of the air compressor for the automotive PEMFC is presented to keep the system in an efficient and orderly operation in the life cycle including the fuel cell performance degradation. A case study of a detailed system is presented to demonstrate the framework procedure. The multiphase model of the PEMFC system is developed and coupled with the GA to optimize the efficiency of the system under various output powers. The main conclusions are as follows:

(1) To verify the accuracy of the model, the 1-D stack model is validated with experimental test results under two operating conditions (before and after 800 h degradation), considering the effect of degradation on the matching strategies. It is obvious that a great agreement is achieved with a relative error less than 2% in the comparations. Meanwhile, a comparison of the data before and after the 800 h degradation is presented. It is found that the performance of the stack without degradation is 7.4% worse than that of the stack after degradation.

(2) The variation in the characteristics parameters of the compressor significantly affects the efficiency of the PEMFC system, and the system performance can be significantly improved by a suitable compressor operating condition. It is found that the effect of compressor characteristics and stack operating parameters on system efficiency is relatively complex and cannot be summarized by a linear relationship.

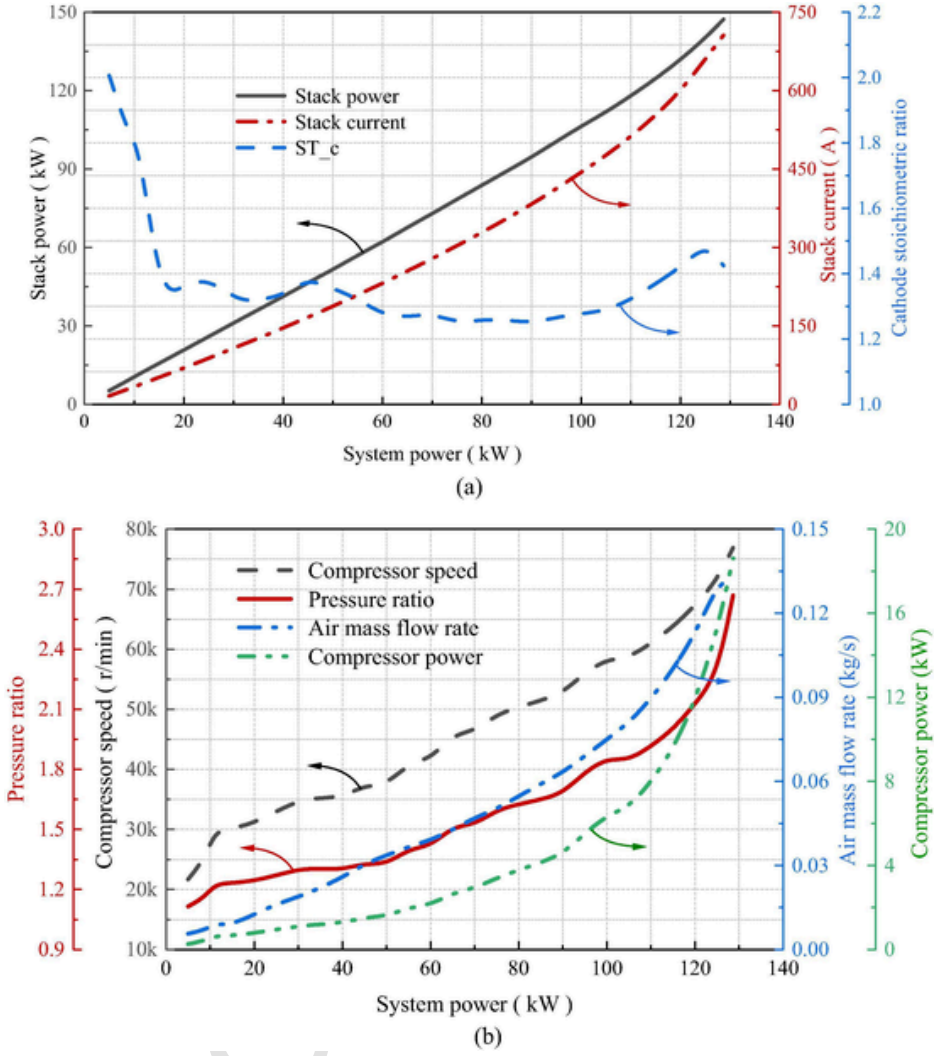


**Fig. 8.** The operating conditions of the stack and air compressor for full system power range, (a) the evolution of the operating parameters of the stack, (b) the evolution of the characteristic parameters of the air compressor.

Consequently, it is essential to investigate the matching strategy of the air compressor and the stack to keep the system with the efficient and orderly operation

(3) With the help of the optimization method, the centrifugal air compressor is matched with the stack to develop the system matching strategies. It is found that the system's efficiency with this optimized method is 3.8% better than the system without the optimized method under the full system power range. The corresponding air compressor speed, pressure ratio, mass flow rate and air compressor parasitic power are rising with the increasing system power progressively. Meanwhile, the growth rate of air compressor pressure ratio, mass flow rate and parasitic power is significantly accelerated with the demand for system power.

(4) In addition, the air compressor is adaptive matched with the stack of the proposed two operating conditions to develop the compressor matching strategies under various stack conditions individually. The new matching strategy between the air compressors and the stack after degradation is developed by the adaptive optimization method. The efficiency of the system and the stack is 5.7% and 2.9% better than that of the matching strategy without adaptive updating. It is found that this adaptive optimization method can not only improve the output efficiency of the stack but also reduce the additional parasitic power consumed by the auxiliary components, which could benefit the durability and performance of the PEMFC system.

## CRediT authorship contribution statement

**Zhichao Gong :** Conceptualization, Methodology, Formal analysis, Writing – original draft, Software. **Bowen Wang :** Methodology, Formal analysis, Writing – review & editing. **Yifan Xu :** Formal analysis, Writing – review & editing. **Meng Ni :** Writing – review & editing. **Qingchen Gao :** Methodology. **Zhongjun Hou :** Supervision, Resources. **Jun Cai :** Resources. **Xin Gu :** Conceptualization, Methodology. **Xinjie Yuan :** Investigation. **Kui Jiao :** Conceptualization, Methodology, Writing – review & editing, Supervision, Resources.

## Declaration of Competing Interest

The authors declare that they have no known competing financial interests or personal relationships that could have appeared to influence the work reported in this paper.

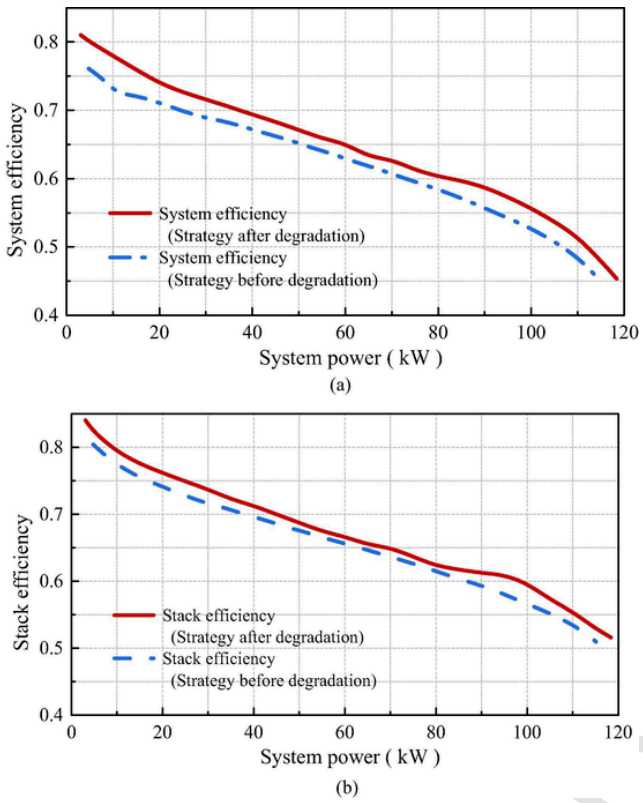


**Fig. 9.** The adaptive optimization results of the stack after degradation, (a) system efficiency, (b) stack efficiency.

**Acknowledgements**

This research is supported by the National Natural Science Foundation of China (grant No. 52176196), China Postdoctoral Science Foundation (No. 2021TQ0235), and Hong Kong Scholars Program (No. XJ2021033). M. Ni also thanks the funding support (Project No: N_PolyU552/20) by Research Grant Council, University Grants Committee, HK SAR, China.



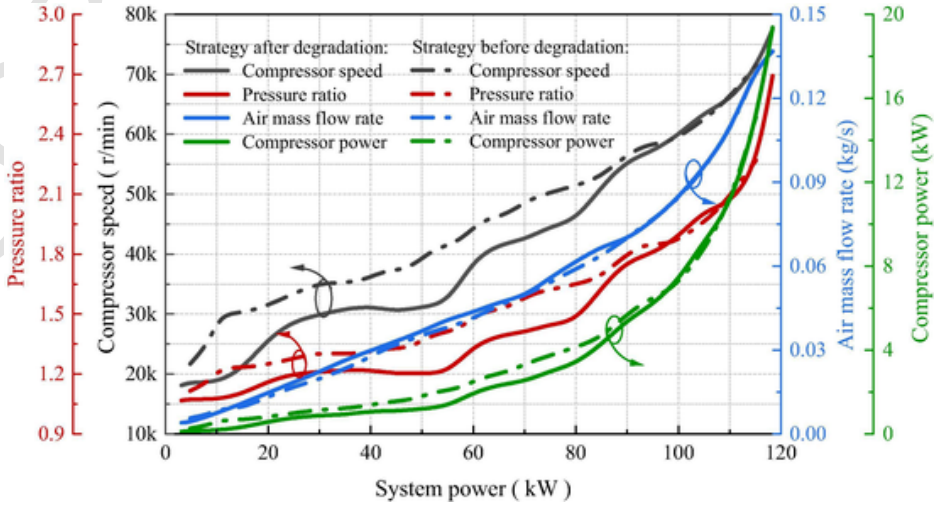


**Fig. 10.** The comparison of the air compressor operating conditions between the previous matching strategy and the adaptive optimization strategy.

## References


[1] Yin C, Song Y, Liu M, Gao Y, Li K, Qiao Z, et al. Investigation of proton exchange membrane fuel cell stack with inversely phased wavy flow field design. Appl Energy 2022;305:117893. https://doi.org/10.1016/j.apenergy.2021.117893.

[2] Jiao K, Xuan J, Du Q, Bao Z, Xie B, Wang B, et al. Designing the next generation of proton-exchange membrane fuel cells. Nature 2021;595(7867):361–9. https://doi.org/10.1038/s41586-021-03482-7.

[3] Yu X, Chang H, Zhao J, Tu Z, Chan S.H. Application of self-adaptive temperature recognition in cold-start of an air-cooled proton exchange membrane fuel cell stack. Energy AI 2022;9:100155. https://doi.org/10.1016/j.egyai.2022.100155.

[4] Song K, Ding Y, Hu X, Xu H, Wang Y, Cao J. Degradation adaptive energy management strategy using fuel cell state-of-health for fuel economy improvement of hybrid electric vehicle. Appl Energy 2021;285(December):116413. https://doi.org/10.1016/j.apenergy.2020.116413.

[5] Benaggoune K, Yue M, Jemei S, Zerhouni N. A data-driven method for multi-step-ahead prediction and long-term prognostics of proton exchange membrane fuel cell. Appl Energy 2022;313:118835. https://doi.org/10.1016/j.apenergy.2022.118835.

[6] Wang B, Zhang G, Wang H, Xuan J, Jiao K. Multi-physics-resolved digital twin of proton exchange membrane fuel cells with a data-driven surrogate model. Energy AI 2020;1:100004. https://doi.org/10.1016/j.egyai.2020.100004.

[7] Li Q.i, Yang W, Yin L, Chen W. Real-time implementation of maximum net power strategy based on sliding mode variable structure control for proton-exchange membrane fuel cell system. IEEE Trans Transp Electrif 2020;6(1):288–97. https://doi.org/10.1109/TTE.2020.2970835.

[8] Yu Y, Chen M, Zaman S, Xing S, Wang M, Wang H. Thermal management system for liquid-cooling PEMFC stack: from primary configuration to system control strategy. eTransportation 2022;12:100165. https://doi.org/10.1016/j.etran.2022.100165.

[9] Yang Z, Du Q, Jia Z, Yang C, Xuan J, Jiao K. A comprehensive proton exchange membrane fuel cell system model integrating various auxiliary subsystems. Appl Energy 2019;256:113959. https://doi.org/10.1016/j.apenergy.2019.113959.

[10] Tao Y, Qiu J, Lai S, Zhang X, Wang G. Collaborative planning for electricity distribution network and transportation system considering hydrogen fuel cell vehicles. IEEE Trans Transp Electrif 2020;6(3):1211–25.

[11] Peng M, Chen L, Zhang R, Xu W, Tao W.-Q. Improvement of thermal and water management of air-cooled polymer electrolyte membrane fuel cells by adding porous media into the cathode gas channel. Electrochim Acta 2022;412(October):140154. https://doi.org/10.1016/j.electacta.2022.140154.

[12] Hu D, Liu J, Yi F, Yang Q, Zhou J. Enhancing heat dissipation to improve efficiency of two-stage electric air compressor for fuel cell vehicle. Energy Convers Manag 2022;251(May):115007. https://doi.org/10.1016/j.enconman.2021.115007.

[13] Zhao D, Xu L, Huangfu Y, Dou M, Liu J. Semi-physical modeling and control of a centrifugal compressor for the air feeding of a PEM fuel cell. Energy Convers Manag 2017;154(August):380–6. https://doi.org/10.1016/j.enconman.2017.11.030.

[14] Chen H, Zhan Z, Jiang P, Sun Y, Liao L, Wan X, et al. Whole life cycle performance degradation test and RUL prediction research of fuel cell MEA. Appl Energy 2022;310:118556. https://doi.org/10.1016/j.apenergy.2022.118556.

[15] Hou J, Yang M, Ke C, Zhang J. Control logics and strategies for air supply in PEM fuel cell engines. Appl Energy 2020;269:115059. https://doi.org/10.1016/j.apenergy.2020.115059.

[16] Li B, Wan K, Xie M, Chu T, Wang X, Li X, et al. Durability degradation mechanism and consistency analysis for proton exchange membrane fuel cell stack. Appl Energy 2022;314:119020. https://doi.org/10.1016/j.apenergy.2022.119020.

[17] Yang Z, Jiao K, Liu Z, Yin Y, Du Q. Investigation of performance heterogeneity of PEMFC stack based on 1 + 1D and flow distribution models. Energy Convers Manag 2020;207:112502. https://doi.org/10.1016/j.enconman.2020.112502.

[18] Shamardina O, Chertovich A, Kulikovsky A.A, Khokhlov A.R. A simple model of a high temperature PEM fuel cell. Int J Hydrogen Energy 2010;35(18):9954–62. https://doi.org/10.1016/j.ijhydene.2009.11.012.

[19] Deng Z, Chen Q, Zhang L, Fu Z. Data driven NARMAX modeling for PEMFC air compressor. Int J Hydrogen Energy 2020;45(39):20321–8. https://doi.org/10.1016/j.ijhydene.2019.11.228.

[20] Zhang Y, Xu S, Wan Y. Performance improvement of centrifugal compressors for fuel cell vehicles using the aerodynamic optimization and data mining methods. Int J Hydrogen Energy 2020;45(19):11276–86. https://doi.org/10.1016/j.ijhydene.2020.02.026.

[21] Zakaria B, Noureddine G, Atallah B, Carlos O.-M. Algebraic observer-based output-feedback controller design for a PEM fuel cell air-supply subsystem. IET Renew Power Gener 2018;12(14):1714–21. https://doi.org/10.1049/iet-rpg.2018.5421.

[22] Liu Z, Chen J, Chen H, Yan C. Air supply regulation for PEMFC systems based on uncertainty and disturbance estimation. Int J Hydrogen Energy 2018;43(25):11559–67. https://doi.org/10.1016/j.ijhydene.2018.01.189.

[23] Wang Y, Wang Y, Xu J, Chai T. Observer-based discrete adaptive neural network control for automotive PEMFC air-feed subsystem. IEEE Trans Veh Technol 2021;70(4):3149–63. https://doi.org/10.1109/TVT.2021.3064604.

[24] Baroud Z, Benmiloud M, Benalia A, Ocampo-Martinez C. Novel hybrid fuzzy-PID control scheme for air supply in PEM fuel-cell-based systems. Int J Hydrogen Energy 2017;42(15):10435–47. https://doi.org/10.1016/j.ijhydene.2017.01.014.

[25] Sun L, Shen J, Hua Q, Lee K.Y. Data-driven oxygen excess ratio control for proton exchange membrane fuel cell. Appl Energy 2018;231(April):866–75. https://doi.org/10.1016/j.apenergy.2018.09.036.

[26] Gong Z, Wang B, Wu K, Miao T, Yang K, Zhai S, et al. A 1 + 1-D Multiphase proton exchange membrane fuel cell model for real-time simulation. IEEE Trans Transp Electrif 2022;8(2):2928–44. https://doi.org/10.1109/TTE.2021.3115794.

[27] Jiang Y, Yang Z, Jiao K, Du Q. Sensitivity analysis of uncertain parameters based on an improved proton exchange membrane fuel cell analytical model. Energy Convers Manag 2018;164(January):639–54. https://doi.org/10.1016/j.enconman.2018.03.002.

[28] Jiao K, Li X. Water transport in polymer electrolyte membrane fuel cells. Prog Energy Combust Sci 2011;37(3):221–91. https://doi.org/10.1016/j.pecs.2010.06.002.

[29] Zawodzinski T.A, Neeman M, Sillerud L.O, Gottesfeld S. Determination of water diffusion coefficients in perfluorosulfonate ionomeric membranes. J Phys Chem 1991;95(15):6040–4. https://doi.org/10.1021/j100168a060.

[30] Jiao K, et al. Water and thermal management of proton exchange membrane fuel cells. Elsevier; 2021. 10.1016/C2020-0-04110-1.

[31] Wei H, Bao H, Ruan X. Perspective: predicting and optimizing thermal transport properties with machine learning methods. Energy AI 2022;8:100153. https://doi.org/10.1016/j.egyai.2022.100153.

[32] Lü X, Wu Y, Lian J, Zhang Y, Chen C, Wang P, et al. Energy management of hybrid electric vehicles: a review of energy optimization of fuel cell hybrid power system based on genetic algorithm. Energy Convers Manag 2020;205:112474. https://doi.org/10.1016/j.enconman.2020.112474.

[33] Wang B, Xie B, Xuan J, Jiao K. AI-based optimization of PEM fuel cell catalyst layers for maximum power density via data-driven surrogate modeling, Energy Convers Manag 2020; 205(December 2019): 112460. doi: 10.1016/j.enconman.2019.112460.

[34] Xu Y, Zhang G, Wu L, Bao Z, Zu B, Jiao K. A 3-D multiphase model of proton exchange membrane electrolyzer based on open-source CFD. Digit Chem Eng 2021;1:100004. https://doi.org/10.1016/j.dche.2021.100004.